

A Distributed Parameter Electromechanical Model for Cantilevered Piezoelectric Energy Harvesters

A. Erturk¹

Center for Intelligent Material Systems
and Structures,
Department of Mechanical Engineering
and Department of Engineering Science
and Mechanics,
Virginia Tech,
Blacksburg, VA 24061
e-mail: erturk@vt.edu

D. J. Inman

Center for Intelligent Material Systems
and Structures,
Department of Mechanical Engineering,
Virginia Tech,
Blacksburg, VA 24061

Cantilevered beams with piezoceramic layers have been frequently used as piezoelectric vibration energy harvesters in the past five years. The literature includes several single degree-of-freedom models, a few approximate distributed parameter models and even some incorrect approaches for predicting the electromechanical behavior of these harvesters. In this paper, we present the exact analytical solution of a cantilevered piezoelectric energy harvester with Euler–Bernoulli beam assumptions. The excitation of the harvester is assumed to be due to its base motion in the form of translation in the transverse direction with small rotation, and it is not restricted to be harmonic in time. The resulting expressions for the coupled mechanical response and the electrical outputs are then reduced for the particular case of harmonic behavior in time and closed-form exact expressions are obtained. Simple expressions for the coupled mechanical response, voltage, current, and power outputs are also presented for excitations around the modal frequencies. Finally, the model proposed is used in a parametric case study for a uni-morph harvester, and important characteristics of the coupled distributed parameter system, such as short circuit and open circuit behaviors, are investigated in detail. Modal electromechanical coupling and dependence of the electrical outputs on the locations of the electrodes are also discussed with examples. [DOI: 10.1115/1.2890402]

Keywords: energy harvesting, piezoelectricity, electromechanical modeling, strain nodes

1 Introduction

For the past five years, there has been an explosion of research in the area of harvesting energy from ambient vibrations by using the direct piezoelectric effect [1]. Research in this area involves understanding the mechanics of vibrating structures, the constitutive behavior of piezoelectric materials, and elementary circuit theory. This promising way of powering small electronic components and remote sensors has attracted researchers from different disciplines of engineering including electrical and mechanical as well as researchers from the field of material science.

The literature includes several experimental demonstrations both in macroscale [2,3] and in microscale [4] piezoelectric energy harvesting. In most of the experimental work, the harvester, which is a cantilevered composite beam with one or more piezoceramic (PZT) layers,² is excited harmonically at its fundamental natural frequency for the maximum electrical output. Although most ambient vibration sources do not have harmonic behavior in time, most previous research has assumed harmonic excitation. Furthermore, in some of the works, the excitation frequency of the harvester is so high that the resulting work deviates from the main motivation of the problem since no such frequencies are available in the ambient energy. Nevertheless, especially in the case of microscale harvesters [4], natural frequencies in the kilohertz frequency band are almost inevitable due to the extremely low mass of the structure.

Many researchers have also focused on the mathematical mod-

eling of these harvesters. A reliable mathematical model may allow studying different aspects of energy harvesting, predicting the electrical outputs, and, moreover, optimizing the harvester for the maximum electrical output for a given input. The modeling approaches in the literature include coupled single degree-of-freedom (SDOF) models [5,6], approximate distributed parameter models (with the Rayleigh–Ritz method) [2,6] as well as some distributed parameter modeling approaches [7,8] that consider a single vibration mode and ignore (or oversimplify) the backward coupling in the mechanical domain and even some incorrect modeling attempts [9] based on informal and weak mathematical modeling assumptions.

The SDOF modeling approach (or the so-called *lumped parameter modeling*) considers the cantilevered beam as a mass-spring-damper system, which is very convenient for coupling the mechanical part of the harvester with a simple electrical harvesting circuit. Although SDOF modeling gives initial insight into the problem by allowing simple closed-form expressions, it is just a simple approximation limited to a single vibration mode of the bender and it lacks several important aspects of the physical system, such as the dynamic mode shape and the accurate strain distribution along the bender. Since these cantilevered harvesters are excited mainly due to the motion of their base, the well-known SDOF harmonic base excitation relation taken from the elementary vibration texts has been frequently referred in the energy harvesting literature both for modeling [6,9] and studying the detailed characteristics [10] of harvesters. Some authors have used the SDOF harmonic base excitation relation just for representing the problem in their experimental work, although they did not provide any detailed mathematical modeling [4,11]. It was recently shown [12] that the traditional form of the SDOF harmonic base excitation relation may yield highly inaccurate results both for transverse and longitudinal vibrations of cantilevered beams and bars depending on the tip (proof) mass to beam/bar mass

¹Corresponding author.

²Here, as a common practice, the abbreviation PZT is used for a generic piezoelectric ceramic, rather than a specific material.

Contributed by the Technical Committee on Vibration and Sound of ASME for publication in the JOURNAL OF VIBRATION AND ACOUSTICS. Manuscript received August 16, 2007; final manuscript received December 7, 2007; published online June 11, 2008. Review conducted by Jeffrey Vipperman.

ratio. When a structure is excited due to the motion of its base, the excitation source is nothing but its own inertia. As a result, the conventional effective mass of cantilevered beams and bars results in underestimation of the predicted response especially if there is low or no tip mass. Erturk and Inman [12] introduced correction factors for improving the existing SDOF harmonic base excitation model for both transverse and longitudinal vibrations of cantilevers.

As an alternative modeling approach, Sodano et al. [2] and duToit et al. [6] used the conventional combination of the variational principle (which is also referred to the Hamilton's principle) and the Rayleigh–Ritz method based on the Euler–Bernoulli beam assumptions. This approximate modeling approach allows predicting the electromechanical response in higher vibration modes. However, it is a numerical approximation technique based on discretization of the continuous distributed parameter system and it is not the exact solution. Other than these approximate techniques, the literature also includes some analytical modeling approaches. In their modeling paper, Lu et al. [7] used a single vibration mode expression (rather than a modal expansion) in the piezoelectric constitutive relation that gives the electric displacement [13] in order to relate the electrical outputs to the mechanical mode shape. Such an approach lacks two important points: backward coupling in the mechanical domain (as coupling in the mechanical equation is not considered) and the contributions from the other vibration modes (as the correct approach implies using the expansion of all vibration modes). Therefore, such a model is *approximately* valid in the vicinity of that respective vibration mode, and the plots given for a wide frequency band (such as the power plot in Ref. [7]) based on this modeling approach are meaningless since all the other vibration modes are missing in the model. Chen et al. [8] also presented a similar distributed parameter modeling approach where the mechanical response was represented by modal expansion, but the effect of backward piezoelectric coupling in the mechanical equation was assumed to be viscous damping. Representing the effect of electromechanical coupling in the mechanical equation by a viscous damping coefficient is a reasonable approach for a certain type of *electromagnetic* harvesters described by Williams and Yates [14] but not for *piezoelectric* harvesters. The effect of piezoelectric coupling in the mechanical domain is more sophisticated than just viscous damping as it results in variation of the natural frequencies rather than just attenuation of the motion amplitude, which is discussed in this paper extensively. Quite recently, Ajitsaria et al. [9] proposed a modeling approach for “bimorph piezoelectric cantilever for voltage generation.” Their main reference considers *static* modeling of piezoelectric actuators where it is reasonable to assume a constant radius of curvature over the beam length. However, Ajitsaria et al. [9] tried to combine these static modeling equations (with constant radius of curvature and static tip force) with the *dynamic* Euler–Bernoulli beam equation (where the radius of curvature varies) and base excitation (where there is no tip force).

In this paper, we present the exact electromechanical solution of a cantilevered piezoelectric energy harvester for transverse vibrations with Euler–Bernoulli beam assumptions. The harvester beam is assumed to be excited by the motion of its base, which is represented by translation in the transverse direction and small rotation. First, the base motion is not restricted to be harmonic in time so that the general coupled equations are obtained for the mechanical response of the beam and the voltage output. Then, the resulting equations are reduced for the case of harmonic base translation with superimposed harmonic small rotation. Closed-form expressions for the voltage, current, and power outputs as well as the mechanical response are presented. The expressions are further reduced to single-mode relations for the case of excitation around a natural frequency of the bender.

We consider more sophisticated damping mechanisms in mechanical modeling of the harvester. The internal strain rate damping (i.e., Kelvin–Voigt damping) and the external air damping

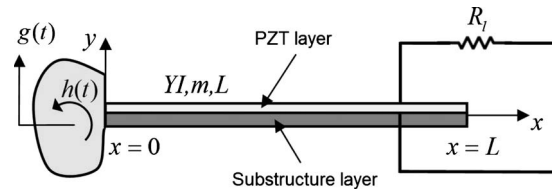


Fig. 1 Unimorph piezoelectric energy harvester under translational and small rotational base motions

effects are treated more accurately by defining separate damping coefficients. The electrical circuit consists of a resistive load connected to the electrodes bracketing the PZT layer. Therefore, along with the internal capacitance of PZT, the electrical circuit is a first order (*RC*) circuit. Although the harvester is taken as a unimorph, the formulation for a bimorph can easily be obtained by following a similar procedure.

The analytically obtained electromechanical expressions are used in a parametric case study where certain electromechanical frequency response functions (FRFs) are defined for graphical demonstration. Voltage, current, power, and relative tip motion FRFs are plotted against frequency for a wide range of load resistance, and the resulting trends in the plots are investigated in detail. Although the mathematical model assumes proportional damping, how to relax this assumption is explained briefly along with a short discussion of how to extract the internal strain rate and external air damping coefficients from experimental measurements. Short circuit and open circuit conditions of the FRFs are discussed and the electromechanical outputs are also plotted against load resistance for these extreme conditions of the resistive load. Finally, the importance of modal electromechanical coupling in energy harvesting is highlighted and its dependence on the locations of the electrodes is discussed. The relevance of the modal coupling concept and the locations of the electrodes to the issue of strain nodes of vibration modes, which was previously discussed [12] and experimentally verified [15], is demonstrated here with FRFs.

2 Derivation of the Electromechanical Model

We consider the unimorph harvester shown in Fig. 1, which is simply a uniform composite Euler–Bernoulli beam consisting of a PZT layer perfectly bonded to the substructure layer. As well known, another typical harvesting configuration is a bimorph with two PZT layers and that configuration can also be modeled in a similar manner by following the below modeling procedure. The harvester shown in Fig. 1 is connected to the electrical circuit through the electrodes, which bracket the PZT layer. The electrodes are assumed to be perfectly conductive and they cover the entire surface of the PZT at the bottom and at the top (so that the electric field is uniform over the length of the beam). The simple electrical circuit consists of a resistive load only. We assume persistent excitation at the base of the harvester so that continuous electrical outputs can be extracted from the resistive load. In general, the leakage resistance of the PZT is much higher than the load resistance, which allows neglecting it in the electrical circuit as it is normally connected to the circuit in parallel to the resistive load. In Fig. 1, the capacitance of the PZT is considered as internal to the PZT rather than showing it as an external element parallel to the resistive load. As we will see later in this work, the piezoelectric constitutive relations [13] generate the electrical capacitance term. Therefore, although it is not shown in Fig. 1 as an element parallel to the resistive load, the capacitance of the PZT layer is not ignored and it will simply show up in the circuit equation.

The harvester beam is typically excited due to the motion of its

base. If the translation and the small rotation of the base are denoted by $g(t)$ and $h(t)$, respectively, then the base motion $w_b(x, t)$ on the beam can be represented as [16]

$$w_b(x, t) = g(t) + xh(t) \quad (1)$$

The governing equation of motion can then be written as [12]

$$\begin{aligned} \frac{\partial^2 M(x, t)}{\partial x^2} + c_s I \frac{\partial^5 w_{\text{rel}}(x, t)}{\partial x^4 \partial t} + c_a \frac{\partial w_{\text{rel}}(x, t)}{\partial t} + m \frac{\partial^2 w_{\text{rel}}(x, t)}{\partial t^2} \\ = -m \frac{\partial^2 w_b(x, t)}{\partial t^2} - c_a \frac{\partial w_b(x, t)}{\partial t} \end{aligned} \quad (2)$$

where $w_{\text{rel}}(x, t)$ is the transverse deflection of the beam relative to its base, $M(x, t)$ is the internal bending moment, $c_s I$ is the equivalent damping term of the composite cross section due to structural viscoelasticity (c_s is the equivalent coefficient of strain rate damping and I is the equivalent area moment of inertia of the composite cross section), c_a is the viscous air damping coefficient, and m is the mass per unit length of the beam. Both of the damping mechanisms considered in the model satisfy the proportional damping criterion, hence, they are mathematically convenient for the modal analysis solution procedure [17]. The strain rate damping indeed shows itself as an internal moment ($M_s = c_s I \partial^3 w_{\text{rel}} / \partial x^2 \partial t$) in the resulting equation of motion. For convenience, we consider it directly outside the internal moment term in Eq. (2); hence, it appears as a separate term.

The internal moment can be obtained by integrating the first moment of the stress distribution at a cross section over the cross-sectional area. The piezoelectric constitutive relations [13] give the stress-strain (and electric field) relations and they are expressed for the substructure and the PZT layers as

$$T_1^s = Y_s S_1^s \quad (3)$$

$$T_1^p = Y_p (S_1^p - d_{31} E_3) \quad (4)$$

respectively. Here, T is the stress, S is the strain, Y is Young's modulus; d is the piezoelectric constant, and E is the electric field. Equation (4) is obtained from the piezoelectric constitutive relation $S_1 = s_{11}^E T_1 + d_{31} E_3$, where s_{11}^E is the elastic compliance at constant electric field and therefore Y_p is simply the reciprocal of s_{11}^E . Furthermore, subscript/superscript p and s stand for PZT and substructure layers, respectively; 1 and 3 directions are coincident with x and y directions, respectively (where 1 is the direction of axial strain and 3 is the direction of polarization). Then, the internal moment can be written as

$$M(x, t) = - \int_{h_a}^{h_b} T_1^s b y dy - \int_{h_b}^{h_c} T_1^p b y dy \quad (5)$$

where b is the width of the beam, h_a is the position of the bottom of the substructure layer from the neutral axis, h_b is the position of the bottom of the PZT layer (therefore, top of the substructure layer) from the neutral axis, and h_c is the position of the top of the PZT layer from the neutral axis (see the Appendix). Expressing the bending strain in terms of radius of curvature [18] and employing Eqs. (3) and (4) in Eq. (5) give

$$\begin{aligned} M(x, t) = \int_{h_a}^{h_b} Y_s b \frac{\partial^2 w_{\text{rel}}(x, t)}{\partial x^2} y^2 dy + \int_{h_b}^{h_c} Y_p b \frac{\partial^2 w_{\text{rel}}(x, t)}{\partial x^2} y^2 dy \\ - \int_{h_b}^{h_c} v(t) Y_p b \frac{d_{31}}{h_p} y dy \end{aligned} \quad (6)$$

where the uniform electric field is written in terms of the voltage $v(t)$ across the PZT and the thickness h_p of the PZT ($E_3(t) = -v(t)/h_p$). Equation (6) can be reduced to

$$M(x, t) = YI \frac{\partial^2 w_{\text{rel}}(x, t)}{\partial x^2} + \vartheta v(t) \quad (7)$$

where YI is the bending stiffness of the composite cross section given by

$$YI = b \left[\frac{Y_s (h_b^3 - h_a^3) + Y_p (h_c^3 - h_b^3)}{3} \right] \quad (8)$$

and the coupling term ϑ can be written as

$$\vartheta = - \frac{Y_p d_{31} b}{2h_p} (h_c^2 - h_b^2) \quad (9)$$

If the PZT layer and/or the electrodes do not cover the entire length of the beam but the region $x_1 \leq x \leq x_2$, then the second term in Eq. (7) should be multiplied by $H(x - x_1) - H(x - x_2)$, where $H(x)$ is the Heaviside function. Note that, in energy harvesting from higher vibration modes, it becomes necessary to use segmented electrode pairs in order to avoid cancellation of the charge collected by continuous electrode pairs [15]. In such a case, one needs to define separate voltage terms, which should appear in Eq. (7) as separate terms multiplied by Heaviside functions. However, in our case, we assume that the electrodes and the PZT layer cover the entire length of the beam displayed in Fig. 1 and it is convenient to rewrite Eq. (7) as

$$M(x, t) = YI \frac{\partial^2 w_{\text{rel}}(x, t)}{\partial x^2} + \vartheta v(t) [H(x) - H(x - L)] \quad (10)$$

where L is the length of the beam. In Eq. (10), although the PZT layer and the electrodes cover the entire beam length, Heaviside functions are associated with the second term in Eq. (10) in order to ensure the survival of this term when the internal moment expression $M(x, t)$ is used in the differential equation of motion given by Eq. (2). Then, employing Eq. (10) in Eq. (2) yields

$$\begin{aligned} YI \frac{\partial^4 w_{\text{rel}}(x, t)}{\partial x^4} + c_s I \frac{\partial^5 w_{\text{rel}}(x, t)}{\partial x^4 \partial t} + c_a \frac{\partial w_{\text{rel}}(x, t)}{\partial t} + m \frac{\partial^2 w_{\text{rel}}(x, t)}{\partial t^2} + \vartheta v(t) \\ \times \left[\frac{d\delta(x)}{dx} - \frac{d\delta(x - L)}{dx} \right] = -m \frac{\partial^2 w_b(x, t)}{\partial t^2} - c_a \frac{\partial w_b(x, t)}{\partial t} \end{aligned} \quad (11)$$

where $\delta(x)$ is the Dirac delta function and it satisfies [19]

$$\int_{-\infty}^{\infty} \frac{d^n \delta(x - x_0)}{dx^n} f(x) dx = (-1)^n \frac{d^n f(x_0)}{dx^n} \quad (12)$$

Equation (11) is the mechanical equation of motion with electrical coupling. In order to obtain the electrical circuit equation with mechanical coupling, one should consider the following piezoelectric constitutive relation:

$$D_3 = d_{31} T_1 + \epsilon_{33}^T E_3 \quad (13)$$

where D_3 is the electric displacement and ϵ_{33}^T is the permittivity at constant stress. If we rearrange Eq. (13) to express axial stress T_1 in terms of bending strain S_1 and Young's modulus of PZT ($Y_p = 1/s_{11}^E$), permittivity component must be replaced by permittivity at constant strain, which is given by $\epsilon_{33}^S = \epsilon_{33}^T - d_{31}^2 Y_p$ [13]. After writing the electric field in the PZT in terms of the voltage across the PZT (that is, $E_3(t) = -v(t)/h_p$), one obtains

$$D_3(x, t) = d_{31} Y_p S_1(x, t) - \epsilon_{33}^S \frac{v(t)}{h_p} \quad (14)$$

The average bending strain at position x and time t in the PZT layer can be expressed as a function of the distance h_{pc} of the center of the PZT layer (in thickness direction) to the neutral axis (see the Appendix) and curvature of the beam at position x and time t ,

$$S_1(x, t) = -h_{pc} \frac{\partial^2 w_{rel}(x, t)}{\partial x^2} \quad (15)$$

Therefore, Eq. (14) becomes

$$D_3(x, t) = -d_{31}Y_p h_{pc} \frac{\partial^2 w_{rel}(x, t)}{\partial x^2} - \varepsilon_{33}^S \frac{v(t)}{h_p} \quad (16)$$

The electric charge $q(t)$ developed in the PZT (and collected by the electrodes) can be obtained by integrating the electric displacement over the electrode area as [13]

$$q(t) = \int_A \mathbf{D} \cdot \mathbf{n} dA = - \int_{x=0}^L \left(d_{31}Y_p h_{pc} b \frac{\partial^2 w_{rel}(x, t)}{\partial x^2} + \varepsilon_{33}^S b \frac{v(t)}{h_p} \right) dx \quad (17)$$

where \mathbf{D} is the vector of electric displacements and \mathbf{n} is the unit outward normal. Clearly, the nonzero terms of these vectors are the ones in 3 direction (i.e., in the y-direction). Then, the current generated by the PZT can be given by

$$i(t) = \frac{dq(t)}{dt} = - \int_{x=0}^L d_{31}Y_p h_{pc} b \frac{\partial^3 w_{rel}(x, t)}{\partial x^2 \partial t} dx - \frac{\varepsilon_{33}^S b L}{h_p} \frac{dv(t)}{dt} \quad (18)$$

Here, the current generated is a function with two components: The first component is due to the vibratory motion of the beam and the second component includes the voltage across the PZT. It is obvious from Eq. (18) that the second term is due to the static capacitance of the PZT. In the literature, the term $\varepsilon_{33}^S b L / h_p$ is called the capacitance of the PZT layer (in general, it is denoted by C_p) and this capacitance is connected to the resistive load (R_l) shown in Fig. 1 in parallel although, physically, the capacitance of the PZT is internal to the PZT itself. Since the current expression given by Eq. (18) includes the capacitance information of the PZT, in this model, it is convenient to connect the PZT directly to the resistive load as a current source without any external capacitive element as we did in Fig. 1. Then, the voltage across the resistive load is simply

$$v(t) = R_l i(t) = -R_l \left[\int_{x=0}^L d_{31}Y_p h_{pc} b \frac{\partial^3 w_{rel}(x, t)}{\partial x^2 \partial t} dx + \frac{\varepsilon_{33}^S b L}{h_p} \frac{dv(t)}{dt} \right] \quad (19)$$

or alternately the electrical circuit equation can be written as

$$\frac{\varepsilon_{33}^S b L}{h_p} \frac{dv(t)}{dt} + \frac{v(t)}{R_l} = - \int_{x=0}^L d_{31}Y_p h_{pc} b \frac{\partial^3 w_{rel}(x, t)}{\partial x^2 \partial t} dx \quad (20)$$

where $v(t)$ is the voltage across the resistive load.

Equations (11) and (20) are the distributed parameter electromechanical equations for a cantilevered piezoelectric energy harvester in transverse vibrations.

3 General Transient Base Motions

The aim of this section is to provide the formal solution procedure of the electromechanically coupled equations of a harvester beam, which are Eqs. (11) and (20). The relative vibratory motion of the beam can be represented by an absolutely and uniformly convergent series of the eigenfunctions as

$$w_{rel}(x, t) = \sum_{r=1}^{\infty} \phi_r(x) \eta_r(t) \quad (21)$$

where $\phi_r(x)$ and $\eta_r(t)$ are the mass normalized eigenfunction and the modal coordinate of the clamped-free beam for the r th mode, respectively. Since the system is proportionally damped, the eigenfunctions denoted by $\phi_r(x)$ are indeed the mass normalized

eigenfunctions of the corresponding *undamped* free vibration problem [17] given by

$$\phi_r(x) = \sqrt{\frac{1}{mL}} \left[\cosh \frac{\lambda_r}{L} x - \cos \frac{\lambda_r}{L} x - \sigma_r \left(\sinh \frac{\lambda_r}{L} x - \sin \frac{\lambda_r}{L} x \right) \right] \quad (22)$$

where the λ_r 's are the dimensionless frequency numbers obtained from the characteristic equation given by

$$1 + \cos \lambda \cosh \lambda = 0 \quad (23)$$

and σ_r is expressed as

$$\sigma_r = \frac{\sinh \lambda_r - \sin \lambda_r}{\cosh \lambda_r + \cos \lambda_r} \quad (24)$$

Note that, for the sake of completeness, the tip mass (or the so-called proof mass) is excluded and the above expressions are for a cantilevered beam without a tip mass. The effect of a tip mass on the resulting formulation of the base excitation problem as well as the respective expressions for the eigenfunctions and the characteristic equation can be found in a recent paper by Erturk and Inman [20].

The mass normalized form of the eigenfunctions given by Eq. (22) satisfies the following orthogonality conditions:

$$\int_{x=0}^L m \phi_s(x) \phi_r(x) dx = \delta_{rs}, \quad \int_{x=0}^L Y I \phi_s(x) \frac{d^4 \phi_r(x)}{dx^4} dx = \omega_r^2 \delta_{rs} \quad (25)$$

where δ_{rs} is the Kronecker delta, defined as being equal to unity for $s=r$ and equal to zero for $s \neq r$, and ω_r is the undamped natural frequency of the r th mode given by

$$\omega_r = \lambda_r^2 \sqrt{\frac{YI}{mL^4}} \quad (26)$$

Using Eq. (21) in the partial differential equation of motion along with the orthogonality conditions given by Eq. (25), the electromechanically coupled ordinary differential equation for the modal response of the beam can be obtained as

$$\frac{d^2 \eta_r(t)}{dt^2} + 2\zeta_r \omega_r \frac{d\eta_r(t)}{dt} + \omega_r^2 \eta_r(t) + \chi_r v(t) = N_r(t) \quad (27)$$

where

$$\chi_r = \vartheta \left. \frac{d\phi_r(x)}{dx} \right|_{x=L} \quad (28)$$

is the modal coupling term and

$$\zeta_r = \frac{c_s I \omega_r}{2YI} + \frac{c_a}{2m\omega_r} \quad (29)$$

is the mechanical damping ratio that includes the effects of both strain rate damping and viscous air damping [12]. It is clear from Eq. (29) that strain rate damping is assumed to be proportional to the bending stiffness of the beam, whereas air damping is assumed to be proportional to the mass per unit length of the beam.

The modal mechanical forcing function $N_r(t)$ can be expressed as

$$N_r(t) = N_r^m(t) + N_r^c(t) \quad (30)$$

Here, the components of mechanical excitation (which are the inertial and the damping excitation terms) are given by the following expressions, respectively;³

³If the excitation due to the external damping of the medium (which is generally air) is negligible when compared to the inertial excitation (i.e., $N_r^c(t) \ll N_r^m(t)$), one can simply set it equal to zero ($N_r^c(t)=0$).

$$N_r^m(t) = -m \left(\gamma_r^w \frac{d^2 g(t)}{dt^2} + \gamma_r^\theta \frac{d^2 h(t)}{dt^2} \right), \quad (31)$$

$$N_r^c(t) = -c_a \left(\gamma_r^w \frac{dg(t)}{dt} + \gamma_r^\theta \frac{dh(t)}{dt} \right)$$

where

$$\gamma_r^w = \int_{x=0}^L \phi_r(x) dx, \quad \gamma_r^\theta = \int_{x=0}^L x \phi_r(x) dx \quad (32)$$

The modal response (that is, the solution of the ordinary differential equation given by Eq. (27)) can be expressed using the Duhamel integral as

$$\eta_r(t) = \frac{1}{\omega_{rd}} \int_{\tau=0}^t [N_r(\tau) - \chi_r v(\tau)] e^{-\zeta_r \omega_r(t-\tau)} \sin \omega_{rd}(t-\tau) d\tau \quad (33)$$

where $\omega_{rd} = \omega_r \sqrt{1-\zeta_r^2}$ is the damped natural frequency of the r th mode. Clearly, obtaining $\eta_r(t)$ from Eq. (33) implies knowing the voltage $v(t)$ across the PZT.

Consider Eq. (20), which is a first order ordinary differential equation for $v(t)$, whose forcing term is a function of the relative vibratory motion. Using Eq. (21) in Eq. (20) yields

$$\frac{dv(t)}{dt} + \frac{h_p}{R_l \epsilon_{33}^S b L} v(t) = \sum_{r=1}^{\infty} \varphi_r \frac{d\eta_r(t)}{dt} \quad (34)$$

where

$$\varphi_r = -\frac{d_{31} Y_p h_{pc} h_p}{\epsilon_{33}^S L} \int_{x=0}^L \frac{d^2 \phi_r(x)}{dx^2} dx = -\frac{d_{31} Y_p h_{pc} h_p}{\epsilon_{33}^S L} \left. \frac{d\phi_r(x)}{dx} \right|_{x=L} \quad (35)$$

Equation (34) can be solved for $v(t)$ by using the following integrating factor:

$$\Psi(t) = e^{t/\tau_c} \quad (36)$$

where τ_c is the time constant of the circuit given by

$$\tau_c = \frac{R_l \epsilon_{33}^S b L}{h_p} \quad (37)$$

Multiplying both sides of Eq. (34) by the integration factor and solving the resulting equation yield the following expression for the voltage across the resistive load:

$$v(t) = e^{-t/\tau_c} \left(\int e^{t/\tau_c} \sum_{r=1}^{\infty} \varphi_r \frac{d\eta_r(t)}{dt} dt + c \right) \quad (38)$$

where c is an arbitrary constant that depends on the initial value of the voltage $v(t)$ across the resistive load as well as the initial velocity of the beam. However, the form of Eq. (33) assumes the initial displacement and the velocity of the beam to be zero (a more complicated form of it could handle the initial displacement and velocity terms). Therefore, since we assume zero initial conditions for the mechanical domain, the term c in Eq. (38) depends only on the initial value of the voltage across the resistive load. Hence, if the initial voltage is zero ($v(0)=0$), simply, $c=0$ and this is what we assume for the sake of simplicity.⁴

Then, if the summation and the integral are switched in Eq. (38), and for $c=0$, one obtains

⁴Yet, one can obtain the value of c for nonzero initial conditions both in the mechanical domain (for the beam) and in the electrical domain (for the electrical circuit). Note that, for nonzero initial conditions in the mechanical domain, the Duhamel integral given by Eq. (33) for the modal mechanical response must be modified accordingly (i.e., initial displacement and velocity terms must be introduced).

$$v(t) = e^{-t/\tau_c} \sum_{r=1}^{\infty} \varphi_r \int e^{t/\tau_c} \frac{d\eta_r(t)}{dt} dt \quad (39)$$

Now, consider the resulting coupled equations (in time domain), which are given by Eqs. (33) and (39). One can either eliminate the voltage term $v(t)$ or the modal mechanical response term $\eta_r(t)$ in order to obtain a single equation in $v(t)$ or $\eta_r(t)$. Eliminating $\eta_r(t)$ and obtaining a single expression for $v(t)$ is preferable for the energy harvesting problem. When the modal mechanical response is eliminated in Eq. (39), one obtains the following implicit expression for the voltage across the resistive load:

$$v(t) = e^{-t/\tau_c} \sum_{r=1}^{\infty} \frac{\varphi_r}{\omega_{rd}} \int e^{t/\tau_c} \frac{d}{dt} \left(\int_{\tau=0}^t [N_r(\tau) - \chi_r v(\tau)] \times e^{-\zeta_r \omega_r(t-\tau)} \sin \omega_{rd}(t-\tau) d\tau \right) dt \quad (40)$$

When the voltage term is eliminated in Eq. (33), one obtains the following implicit equation for the modal response:

$$\eta_r(t) = \frac{1}{\omega_{rd}} \int_{\tau=0}^t \left[N_r(\tau) - \chi_r e^{-\tau/\tau_c} \sum_{r=1}^{\infty} \varphi_r \int e^{\tau/\tau_c} \frac{d\eta_r(\tau)}{d\tau} d\tau \right] \times e^{-\zeta_r \omega_r(t-\tau)} \sin \omega_{rd}(t-\tau) d\tau \quad (41)$$

The solution of Eq. (41) for $\eta_r(t)$ can be used in Eq. (21) to obtain the coupled physical response of the beam.

4 Harmonic Base Motion (Translation With Small Rotation) at an Arbitrary Frequency

In this section, we assume the translation and small rotation of the beam to be harmonic in time (i.e., $g(t) = Y_0 e^{j\omega t}$ and $h(t) = \theta_0 e^{j\omega t}$, where Y_0 and θ_0 are the amplitudes of the base translation and rotation, respectively, ω is the driving frequency, and $j = \sqrt{-1}$ is the unit imaginary number) and obtain closed-form expressions for steady state voltage output and beam response. Since the electromechanical system is assumed to be linear, we expect the voltage output to be harmonic also in the form of $v(t) = V_0 e^{j\omega t}$ (where V_0 is the amplitude of the harmonic voltage across the resistive load). Then, the modal equation of motion given by Eq. (27) can be reduced to⁵

$$\frac{d^2 \eta_r(t)}{dt^2} + 2\zeta_r \omega_r \frac{d\eta_r(t)}{dt} + \omega_r^2 \eta_r(t) + \chi_r V_0 e^{j\omega t} = m\omega^2 (\gamma_r^w Y_0 + \gamma_r^\theta \theta_0) e^{j\omega t} \quad (42)$$

The steady state solution of Eq. (42) can be expressed as

$$\eta_r(t) = \frac{[m\omega^2 (\gamma_r^w Y_0 + \gamma_r^\theta \theta_0) - \chi_r V_0] e^{j\omega t}}{\omega_r^2 - \omega^2 + j2\zeta_r \omega_r \omega} \quad (43)$$

It is important to note that the input in the energy harvesting problem is the base motion $w_b(x, t) = (Y_0 + x\theta_0) e^{j\omega t}$ and the output is the voltage across the resistive load $v(t) = V_0 e^{j\omega t}$. Although they look like two separate forcing terms in Eq. (43), $v(t)$ is indeed induced due to $w_b(x, t)$, but it acts back as a forcing term in the mechanical equation due to the electromechanical coupling. Furthermore, $v(t)$ and $w_b(x, t)$ do not have to be in phase, which makes V_0 complex valued although Y_0 and θ_0 are real valued.

⁵Excitation due to air damping is ignored.

For the electrical circuit, from Eq. (34), one obtains

$$\left(\frac{1+j\omega\tau_c}{\tau_c}\right)V_0 e^{j\omega t} = \sum_{r=1}^{\infty} \varphi_r \frac{d\eta_r(t)}{dt} \quad (44)$$

Then, using Eq. (43) in Eq. (44), one can eliminate $\eta_r(t)$ and obtain the following implicit expression for the voltage amplitude V_0 across the load resistance:

$$\left(\frac{1+j\omega\tau_c}{\tau_c}\right)V_0 = \sum_{r=1}^{\infty} \varphi_r \frac{j\omega[m\omega^2(\gamma_r^w Y_0 + \gamma_r^\theta \theta_0) - \chi_r V_0]}{\omega_r^2 - \omega^2 + j2\zeta_r \omega_r \omega} \quad (45)$$

However, it is now straightforward to express V_0 explicitly as

$$V_0 = \frac{\sum_{r=1}^{\infty} \frac{j m \omega^3 \varphi_r (\gamma_r^w Y_0 + \gamma_r^\theta \theta_0)}{\omega_r^2 - \omega^2 + j2\zeta_r \omega_r \omega}}{\sum_{r=1}^{\infty} \frac{j \omega \chi_r \varphi_r}{\omega_r^2 - \omega^2 + j2\zeta_r \omega_r \omega} + \frac{1+j\omega\tau_c}{\tau_c}} \quad (46)$$

which is the amplitude of the voltage across the resistive load. Therefore, the voltage response $v(t)$ (across the resistive load) due to the harmonic base motion $w_b(x,t) = (Y_0 + x\theta_0)e^{j\omega t}$ can be expressed as

$$v(t) = \frac{\sum_{r=1}^{\infty} \frac{j m \omega^3 \varphi_r (\gamma_r^w Y_0 + \gamma_r^\theta \theta_0) e^{j\omega t}}{\omega_r^2 - \omega^2 + j2\zeta_r \omega_r \omega}}{\sum_{r=1}^{\infty} \frac{j \omega \chi_r \varphi_r}{\omega_r^2 - \omega^2 + j2\zeta_r \omega_r \omega} + \frac{1+j\omega\tau_c}{\tau_c}} \quad (47)$$

Note that, after obtaining the time history of the voltage across the resistive load, one can easily obtain the current generated by the PZT by using $i(t) = v(t)/R_l$. Furthermore, the instantaneous power output can be expressed using the well-known relation $P(t) = v^2(t)/R_l$. It is worthwhile to mention that, due to the similarity between the energy harvesting problem (for persistent vibrations) and the *piezoelectric shunt damping* problem, some of the equations derived here may also be applicable to the multimode shunt damping of a cantilevered beam (see, for instance, Moheimani et al. [21]). Note that the resistive load connected to the leads of the electrodes in the circuit can easily be replaced by the impedance of a more general (but linear) *RLC* circuit and we can obtain closed-form expressions for harmonic excitations as long as the linearity of the electromechanical system is preserved.

It is also possible to eliminate the voltage term in Eq. (43) in order to obtain the modal mechanical response of the beam as

$$\eta_r(t) = \left[(\gamma_r^w Y_0 + \gamma_r^\theta \theta_0) - \chi_r \left(\frac{\sum_{r=1}^{\infty} \frac{j \omega \varphi_r (\gamma_r^w Y_0 + \gamma_r^\theta \theta_0)}{\omega_r^2 - \omega^2 + j2\zeta_r \omega_r \omega}}{\sum_{r=1}^{\infty} \frac{j \omega \chi_r \varphi_r}{\omega_r^2 - \omega^2 + j2\zeta_r \omega_r \omega} + \frac{1+j\omega\tau_c}{\tau_c}} \right) \right] \times \frac{m \omega^2 e^{j\omega t}}{\omega_r^2 - \omega^2 + j2\zeta_r \omega_r \omega} \quad (48)$$

which can be employed in Eq. (21) to obtain the vibratory re-

sponse of the beam relative to its base as

$$w_{\text{rel}}(x,t) = \sum_{r=1}^{\infty} \left[(\gamma_r^w Y_0 + \gamma_r^\theta \theta_0) - \chi_r \left(\frac{\sum_{r=1}^{\infty} \frac{j \omega \varphi_r (\gamma_r^w Y_0 + \gamma_r^\theta \theta_0)}{\omega_r^2 - \omega^2 + j2\zeta_r \omega_r \omega}}{\sum_{r=1}^{\infty} \frac{j \omega \chi_r \varphi_r}{\omega_r^2 - \omega^2 + j2\zeta_r \omega_r \omega} + \frac{1+j\omega\tau_c}{\tau_c}} \right) \right] \times \frac{m \omega^2 \phi_r(x) e^{j\omega t}}{\omega_r^2 - \omega^2 + j2\zeta_r \omega_r \omega} \quad (49)$$

5 Harmonic Base Translation at an Arbitrary Frequency

In the energy harvesting literature, the base excitation is considered as harmonic translation in the transverse direction and the beam is assumed to be not rotating. In such a case (i.e., when $h(t)=0$), the resulting expressions for the steady state voltage response can be reduced to

$$v(t) = \frac{\sum_{r=1}^{\infty} \frac{j m \omega^3 \varphi_r \gamma_r^w}{\omega_r^2 - \omega^2 + j2\zeta_r \omega_r \omega} Y_0 e^{j\omega t}}{\sum_{r=1}^{\infty} \frac{j \omega \chi_r \varphi_r}{\omega_r^2 - \omega^2 + j2\zeta_r \omega_r \omega} + \frac{1+j\omega\tau_c}{\tau_c}} \quad (50)$$

and the vibratory response of the beam relative to its base can be obtained from

$$w_{\text{rel}}(x,t) = \sum_{r=1}^{\infty} \left[\gamma_r^w - \chi_r \left(\frac{\sum_{r=1}^{\infty} \frac{j \omega \varphi_r \gamma_r^w}{\omega_r^2 - \omega^2 + j2\zeta_r \omega_r \omega}}{\sum_{r=1}^{\infty} \frac{j \omega \chi_r \varphi_r}{\omega_r^2 - \omega^2 + j2\zeta_r \omega_r \omega} + \frac{1+j\omega\tau_c}{\tau_c}} \right) \right] \times \frac{m \omega^2 \phi_r(x) Y_0 e^{j\omega t}}{\omega_r^2 - \omega^2 + j2\zeta_r \omega_r \omega} \quad (51)$$

6 Harmonic Base Translation Around a Natural Frequency

If the beam is excited around the natural frequency of the r th mode, the main contributions in the summation signs appearing in Eqs. (50) and (51) are from the r th mode. In most cases, the mode of interest is the fundamental vibration mode of the harvester (i.e., $r=1$). Therefore, it is a useful practice to consider the beam to be excited around ω_1 . The *reduced* expression for the voltage across the resistive load can be written as

$$v^*(t) = \frac{j \tau_c m \omega^3 \varphi_1 \gamma_1^w}{j \omega \tau_c \chi_1 \varphi_1 + (1+j\omega\tau_c)(\omega_1^2 - \omega^2 + j2\zeta_1 \omega_1 \omega)} Y_0 e^{j\omega t} \quad (52)$$

and the reduced expression for vibratory response of the beam relative to its base is

$$w_{\text{rel}}^*(x, t) = \frac{(1 + j\omega\tau_c)m\omega^2\gamma_1^w\phi_1(x)}{j\omega\tau_c\chi_1\varphi_1 + (1 + j\omega\tau_c)(\omega_1^2 - \omega^2 + j2\zeta_1\omega_1\omega)} Y_0 e^{j\omega t} \quad (53)$$

reduced for excitation around a specific vibration mode (which is the fundamental mode in this case).

Equation (52) can be rewritten as

$$v^*(t) = |V_0^*| e^{j(\omega t + \Phi_v)} \quad (54)$$

where the superscript “*” denotes that the respective expression is where the amplitude of the voltage output is (assuming $Y_0 > 0$)

$$|V_0^*| = \frac{\tau_c m \omega^3 Y_0 |\varphi_1 \gamma_1^w|}{\sqrt{[\omega_1^2 - \omega^2(1 + 2\tau_c \zeta_1 \omega_1)]^2 + [2\zeta_1 \omega_1 \omega + \tau_c \omega(\chi_1 \varphi_1 + \omega_1^2 - \omega^2)]^2}} \quad (55)$$

and the phase angle between the base displacement and the reduced voltage output is simply

$$\Phi_v = \frac{\pi}{2} \text{sgn}(\varphi_1 \gamma_1^w) - \tan^{-1} \left(\frac{2\zeta_1 \omega_1 \omega + \tau_c \omega(\chi_1 \varphi_1 + \omega_1^2 - \omega^2)}{\omega_1^2 - \omega^2(1 + 2\tau_c \zeta_1 \omega_1)} \right) \quad (56)$$

where “sgn” is the *signum function*.

Similarly, Eq. (53) can be expressed as

$$w_{\text{rel}}^*(x, t) = |W_{\text{rel}}^*(x)| e^{j(\omega t + \Phi_w)} \quad (57)$$

where the amplitude of the vibratory motion at point x (relative to the base of the beam) can be written as

$$|W_{\text{rel}}^*(x)| = \frac{m\omega^2 Y_0 |\gamma_1^w \phi_1(x)| \sqrt{1 + (\omega\tau_c)^2}}{\sqrt{[\omega_1^2 - \omega^2(1 + 2\tau_c \zeta_1 \omega_1)]^2 + [2\zeta_1 \omega_1 \omega + \tau_c \omega(\chi_1 \varphi_1 + \omega_1^2 - \omega^2)]^2}} \quad (58)$$

and the phase angle between the base displacement and the relative displacement at point x is simply

$$\Phi_w = \tan^{-1} \left(\frac{\omega\tau_c \gamma_1^w \phi_1(x)}{\gamma_1^w \phi_1(x)} \right) - \tan^{-1} \left(\frac{2\zeta_1 \omega_1 \omega + \tau_c \omega(\chi_1 \varphi_1 + \omega_1^2 - \omega^2)}{\omega_1^2 - \omega^2(1 + 2\tau_c \zeta_1 \omega_1)} \right) \quad (59)$$

The reduced expression for the current flow through the resistive load can then be obtained as

$$i^*(t) = |I_0^*| e^{j(\omega t + \Phi_i)} \quad (60)$$

where

$$|I_0^*| = \frac{C_p m \omega^3 Y_0 |\varphi_1 \gamma_1^w|}{\sqrt{[\omega_1^2 - \omega^2(1 + 2\tau_c \zeta_1 \omega_1)]^2 + [2\zeta_1 \omega_1 \omega + \tau_c \omega(\chi_1 \varphi_1 + \omega_1^2 - \omega^2)]^2}} \quad (61)$$

and $\Phi_i = \Phi_v$, i.e., the voltage across the resistive load and the current flow through it are in phase, reasonably. In Eq. (61), C_p is the capacitance of the PZT due to $C_p = \epsilon_{33}^S bL/h_p$ as mentioned previously and $C_p = \tau_c/R_l$ from Eq. (37).

The amplitude of the power output (reduced for the fundamental vibration mode) can then be expressed as

$$|P_0^*| = \frac{C_p \tau_c (m \varphi_1 \gamma_1^w \omega^3 Y_0)^2}{[\omega_1^2 - \omega^2(1 + 2\tau_c \zeta_1 \omega_1)]^2 + [2\zeta_1 \omega_1 \omega + \tau_c \omega(\chi_1 \varphi_1 + \omega_1^2 - \omega^2)]^2} \quad (62)$$

It is important to note that Eqs. (52)–(62) are valid *only* at the excitation frequencies around the first natural frequency of the harvester beam. Replacing the subscript “1” by r in Eqs. (52)–(62), one can obtain the respective electrical and mechanical expressions for excitation frequencies around the r th natural frequency.

7 Parametric Case Study for a Unimorph Harvester

In this section, we analyze the unimorph harvester shown in Fig. 2 by using the proposed distributed parameter model. The

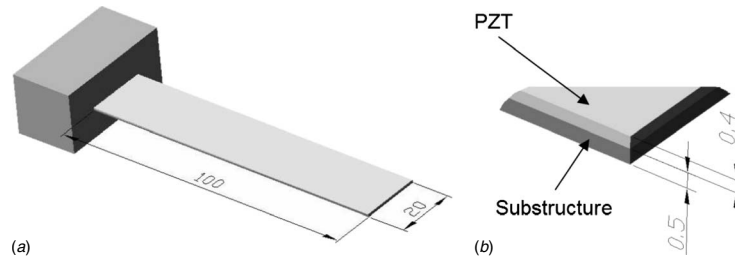


Fig. 2 (a) The unimorph piezoelectric energy harvester used for the parametric case study and (b) a detail from its cross section (dimensions are in millimeters)

Table 1 Geometric, material, and electromechanical parameters of the sample harvester

Length of the beam, L (mm)	100
Width of the beam, b (mm)	20
Thickness of the substructure, h_s (mm)	0.5
Thickness of the PZT, h_p (mm)	0.4
Young's modulus of the substructure, Y_s (GPa)	100
Young's modulus of the PZT, Y_p (GPa)	66
Mass density of the substructure, ρ_s (kg/m ³)	7165
Mass density of the PZT, ρ_p (kg/m ³)	7800
Piezoelectric constant, d_{31} (pm/V)	-190
Permittivity, ϵ_{33}^S (nF/m)	15.93

geometric, material, and the electromechanical parameters of the harvester are given in Table 1. The conductive electrodes bracketing the PZT layer (not shown in Fig. 2) are assumed to be covering the entire length of the harvester beam. The excitation of the harvester is due to the harmonic translation $w_b(t) = Y_0 e^{j\omega t}$ of its base in the transverse direction and we are interested in the steady state dynamic behavior of the system. Rather than specifying certain Y_0 and ω values for the input, it is preferred to obtain the results in terms of these parameters so that it becomes possible to represent the electromechanical outputs as FRFs.

Let the frequency range of interest be 0–1000 Hz. Then, for the parameters given in Table 1, it is straightforward to show that the uncoupled harvester has three natural frequencies lying in this frequency range. The first part of our analysis focuses on the following four important FRFs: voltage across the resistive load, current flow through the resistive load, electrical power output, and the relative motion transmissibility from the base to the tip of the beam. The first three FRFs are for the electrical domain, and clearly, the third one (power output) depends on the first two (voltage and current). The last FRF gives the ratio of the vibration amplitude at the tip of the beam (relative to its base) to the amplitude of the input base translation. Therefore, only the mechanical FRF gives some idea about the electromechanical effects on the beam caused by the energy harvesting circuit at different vibration modes. It is worthwhile to mention that distributed parameter modeling is not limited to the motion at the tip of the beam as the analysis presented here allows predicting the coupled vibration response at any point along the beam.

Due to the electromechanical coupling, each vibration mode has a short circuit resonance frequency ω_r^{sc} (for $R_l \rightarrow 0$) and an open circuit resonance frequency ω_r^{oc} (for $R_l \rightarrow \infty$), where subscript r stands for the mode number. These frequencies are defined for the extreme cases of the resistive load, and for its moderate values, reasonably, the resonance frequency of the respective vibration mode takes values between ω_r^{sc} and ω_r^{oc} . In the below analysis, after plotting each FRF against the excitation frequency, we investigate the short circuit and open circuit behaviors of the outputs by plotting them against the load resistance.

7.1 Identification of Mechanical Damping Coefficients. Before presenting the resulting FRFs and discussing their respective trends, it may be appropriate to add a few words on mechanical damping and evaluation of the mechanical damping coefficients from experimental measurements. With the form of the differential equation of motion given by Eq. (2), we assumed two separate damping terms for the internal (strain rate) and the external viscous (air) damping mechanisms, which are $c_s I$ and c_a , respectively. This is the formal way of treating the problem and a detailed discussion is available in Ref. [12]. As mentioned previously, $c_s I$ is assumed to be stiffness proportional and c_a is assumed to be mass proportional. Evaluating these damping coefficients from experimental measurements requires knowing the frequencies and damping ratios of two separate vibration modes (say, modes m and n) [22]. Then, for $r=m$ and $r=n$, one has two

linear algebraic equations to solve for the unknowns $c_s I$ and c_a (see Eq. (29)). Suppose that, for the harvester of our interest (Fig. 2), we obtain the damping ratios of the first two modes as $\zeta_1 = 0.010$ and $\zeta_2 = 0.013$ from experimental modal analysis under short circuit conditions ($R_l \rightarrow 0$) and this is what we assume for our parametric study. We also know that $\omega_1 = 300.4$ rad/s and $\omega_2 = 1882.5$ rad/s. Then, the two equations coming from Eq. (29) give the proportionality constants as $c_s I / YI = 1.2433 \times 10^{-5}$ s/rad and $c_a / m = 4.886$ rad/s. Once these proportionality constants are used in the mathematical model, the rest of the modal damping ratios are automatically set to the following numbers: $\zeta_3 = 0.033$, $\zeta_4 = 0.064$, $\zeta_5 = 0.106$, and so on. However, one should always keep in mind that proportional damping is a convenient *mathematical* modeling assumption and the *physical* system may not agree with this assumption. In other words, the damping ratios of higher vibration modes may not converge to the above values. At this point, it is important to note that instead of using $c_s I$ and c_a in the distributed parameter model we propose, one can always use the modal damping ratios (ζ_r 's) obtained experimentally directly in the modal expansions appearing in the resulting electromechanical expressions. For example, if the first three modes are of interest, one obtains the damping ratios of these modes experimentally and employs them in the summation terms of the resulting equations by just considering these three modes ($n=3$). This way allows a *relaxation* in the proportional damping assumption and one does not need to obtain the values of $c_s I$ and c_a .

7.2 Frequency Response of Voltage Output. Having discussed some important points regarding the mechanical damping and its accurate evaluation, we start investigating the resulting electromechanical FRFs. Since the value of load resistance R_l is an important parameter that shapes the dynamic behavior of the system, we plot the FRFs for five different orders of magnitude of R_l ranging from $10^2 \Omega$ to $10^6 \Omega$. As discussed previously, short circuit behavior is expected for low values of load resistance ($R_l \rightarrow 0$), whereas the system is expected to move toward the open circuit conditions for large values of load resistance ($R_l \rightarrow \infty$).

The voltage FRF is described as the ratio of the voltage output to the base acceleration. Therefore, this FRF can be extracted from Eq. (50) as

$$\frac{v(t)}{-\omega^2 Y_0 e^{j\omega t}} = \frac{\sum_{r=1}^{\infty} \frac{-jm\omega\varphi_r \gamma_r^w}{\omega_r^2 - \omega^2 + j2\zeta_r \omega_r \omega}}{\sum_{r=1}^{\infty} \frac{j\omega\chi_r \varphi_r}{\omega_r^2 - \omega^2 + j2\zeta_r \omega_r \omega} + \frac{1 + j\omega\tau_c}{\tau_c}} \quad (63)$$

The modulus of the “voltage FRF” given by Eq. (63) is plotted in Fig. 3. As can be seen from Fig. 3, the amplitude of the voltage output increases monotonically with increasing load resistance for all excitation frequencies. Furthermore, with increasing load resistance, the resonance frequency of each vibration mode moves from the short circuit resonance frequency (ω_r^{sc}) to the open circuit resonance frequency (ω_r^{oc}). As an example, the enlarged view of the first resonance is displayed in Fig. 3. For excitation at the first vibration mode, the maximum voltage is obtained for $\omega_1^{sc} = 47.8$ Hz when $R_l = 10^2 \Omega$. However, when $R_l = 10^6 \Omega$ is used, the resonance frequency of the fundamental vibration mode becomes $\omega_1^{oc} = 48.8$ Hz. For every excitation frequency, the maximum voltage output is obtained when the system is close to open circuit conditions. A similar trend (the existence of open circuit and short circuit resonance frequencies) is valid for all vibration modes. Table 2 shows the frequencies of the short circuit and the open circuit resonances for the first three vibration modes.

As mentioned, the voltage output increases monotonically with increasing load resistance at every excitation frequency. The two important excitation frequencies of the fundamental vibration mode are the short circuit and the open circuit resonance frequen-

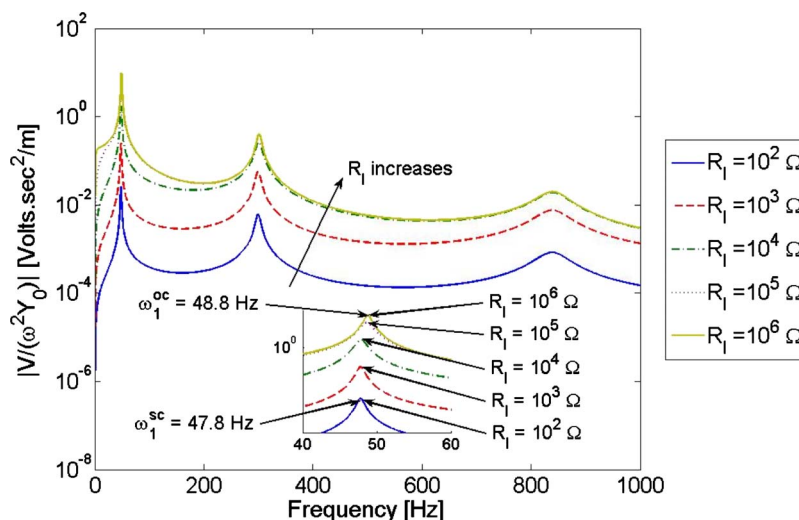


Fig. 3 Voltage FRF for five different values of load resistance (with the enlarged view of Mode 1 resonance showing the short circuit and open circuit behaviors)

cies, which are $\omega_1^{sc}=47.8$ Hz and $\omega_1^{oc}=48.8$ Hz, respectively. Variation of the voltage output with load resistance at these frequencies is shown in Fig. 4. As can be seen from Fig. 4, for low values of load resistance, the voltage outputs at these two particular excitation frequencies increase with the same slope (in log-log scale) and the voltage output at the short circuit resonance frequency is higher since the system is close to short circuit conditions. However, the curves intersect at a certain value of load resistance (around 39.8 k Ω) and for the values of load resistance higher than the value at the intersection point, the voltage output at the open circuit resonance frequency is higher expectedly. The

Table 2 Short circuit and open circuit resonance frequencies of the harvester for the first three vibration modes

	Mode 1	Mode 2	Mode 3
ω_r^{sc} (Hz) (short circuit)	47.8	299.6	838.2
ω_r^{oc} (Hz) (open circuit)	48.8	301.5	839.2

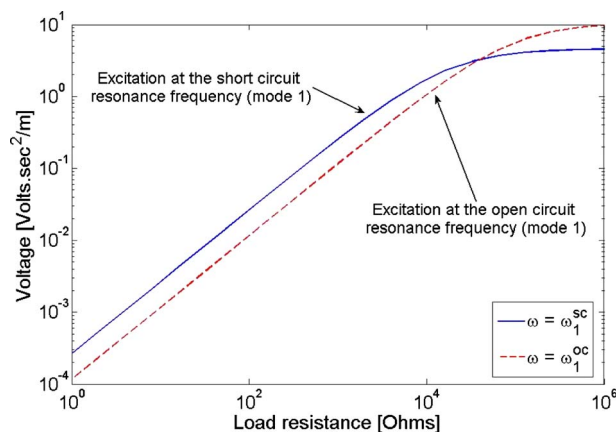


Fig. 4 Variation of voltage output with load resistance for base excitations at the short circuit and open circuit resonance frequencies of the first vibration mode

voltage output becomes less sensitive to the variations in the load resistance at open circuit conditions (i.e., for very large values of load resistance).

7.3 Frequency Response of Current Output. The current FRF can easily be obtained by dividing the voltage FRF by the load resistance as follows:

$$\frac{i(t)}{-\omega^2 Y_0 e^{j\omega t}} = \frac{v(t)}{-R_l \omega^2 Y_0 e^{j\omega t}} = \frac{\sum_{r=1}^{\infty} \frac{-j m \omega \varphi_r \gamma_r^v}{\omega_r^2 - \omega^2 + j 2 \zeta_r \omega_r \omega}}{R_l \left(\sum_{r=1}^{\infty} \frac{j \omega \chi_r \varphi_r}{\omega_r^2 - \omega^2 + j 2 \zeta_r \omega_r \omega} + \frac{1 + j \omega \tau_c}{\tau_c} \right)} \quad (64)$$

The modulus of the current FRF is plotted against frequency in Fig. 5. Unlike the voltage FRF shown in Fig. 3, the amplitude of the current decreases with increasing load resistance. Indeed, this is the opposite of the voltage behavior shown in Fig. 3 but the behavior is still monotonic. For every excitation frequency, the maximum value of the current is obtained when the system is close to short circuit conditions.

Figure 6 shows the current output as a function of load resistance for excitations at the short circuit and the open circuit resonance frequencies of the first mode. It is clear from Fig. 6 that the current is highly insensitive to the variations of the load resistance at the range of its low values (i.e., the slope is almost zero). In this relatively low load resistance region, the current output is higher at the short circuit resonance frequency, as in the case of voltage (Fig. 4), since the system is close to short circuit conditions. Then, current starts decreasing with further increase in load resistance, and at a certain value of load resistance (again, around 39.8 k Ω), the curves intersect. For the values of load resistance higher than the value at this intersection point, the current output at the open circuit resonance frequency becomes higher since the system approaches the open circuit conditions.

7.4 Frequency Response of Power Output. The FRF of the power output is simply the product of the voltage and the current FRFs given by Eqs. (63) and (64), respectively. Therefore, unlike the voltage and the current FRFs, the power output FRF is defined

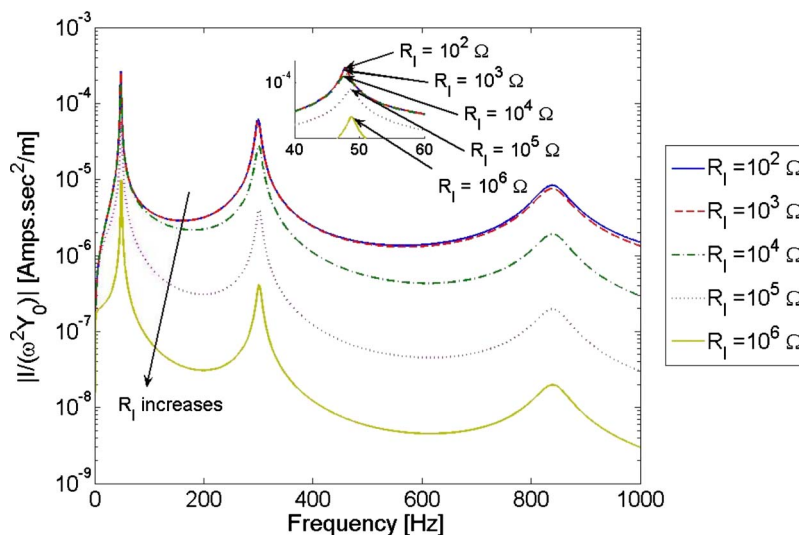


Fig. 5 Current FRF for five different values of load resistance (with the enlarged view of Mode 1 resonance showing the short circuit and open circuit behaviors)

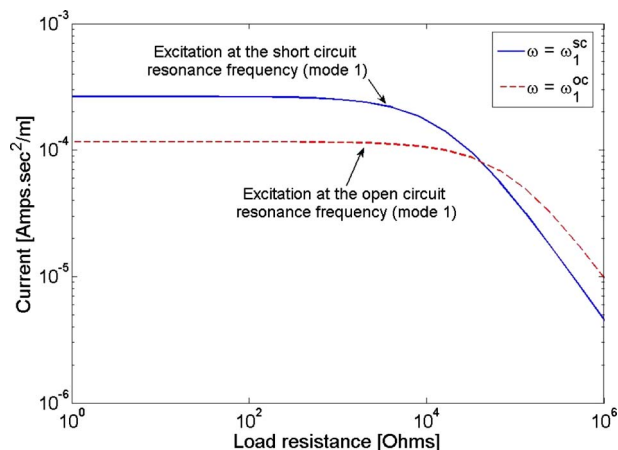


Fig. 6 Variation of current output with load resistance for base excitations at the short circuit and open circuit resonance frequencies of the first vibration mode

as the power divided by the *square* of the base acceleration. The modulus of the power output FRF is displayed in Fig. 7. Since it is the product of two FRFs that have the opposite behaviors with increasing load resistance, the behavior of the power output FRF with load resistance is more interesting than the previous two electrical outputs and it deserves more discussion. It is clear from Fig. 7 that the power output FRF does not exhibit a monotonic behavior with increasing (or decreasing) load resistance. Among the sample values of the load resistance considered in this work, the value of maximum power output for the first vibration mode corresponds to $R_l = 10^5 \Omega$ (see the first enlarged view in Fig. 7) at frequency $\omega = 48.66$ Hz, which is expectedly around the open circuit resonance frequency of the first mode (Table 2) for this relatively large value of load resistance. Considering the second vibration mode (see the second enlarged view in Fig. 7), one observes that the maximum power output is obtained for $R_l = 10^4 \Omega$ at frequency $\omega = 300.88$ Hz and this frequency has a moderate value between the short circuit and the open circuit reso-

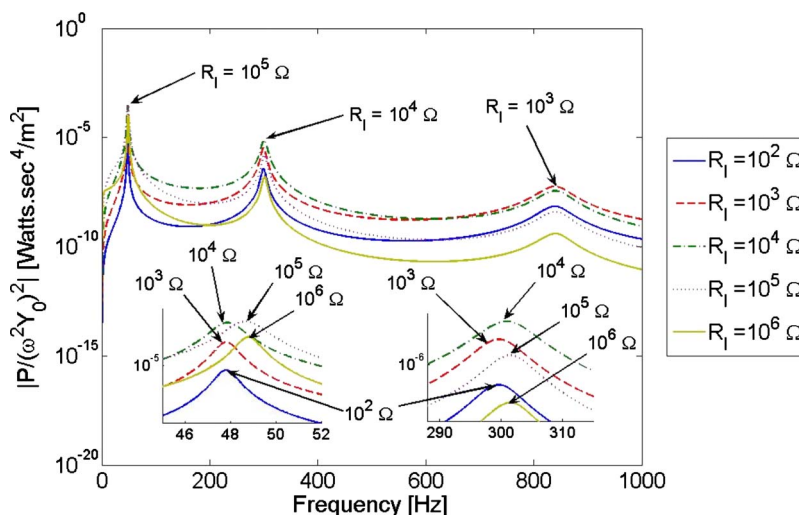


Fig. 7 Power output FRF for five different values of load resistance (with the enlarged views of Mode 1 and Mode 2 resonances showing the short circuit and open circuit behaviors)

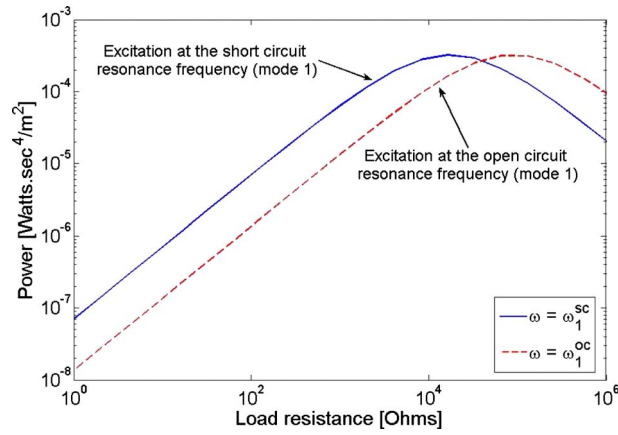


Fig. 8 Variation of power output with load resistance for base excitations at the short circuit and open circuit resonance frequencies of the first vibration mode

nance frequencies of the second vibration mode (Table 2) since the respective resistive load also has a moderate value. According to Fig. 7, among the sample values of load resistance employed in the analysis, the maximum power output for excitation at the third vibration mode corresponds to $R_l = 10^3 \Omega$ at frequency $\omega = 838.34$ Hz, which is close to the short circuit resonance frequency of the third vibration mode (Table 2) as this resistive load has a relatively low value. One should note that the values of the load resistance we use in this analysis are taken arbitrarily to observe the general trends. Therefore, the maximum power outputs obtained from each vibration mode are for these sample values and they are not necessarily the *maximum possible* (or the optimized) power outputs. It is a straightforward practice to obtain the optimum resistive load and its respective resonance frequency for each vibration mode and it is beyond the discussion of this section, which aims to address more general points. Another interesting point to mention is the *switching* between the curves of different values of load resistance, which results in intersections between the FRFs. These intersections are observed not only around the resonance frequencies (see the first enlarged view, e.g., the curves for $R_l = 10^4 \Omega$ and $R_l = 10^5 \Omega$ intersect at 48.19 Hz) but also they are observed at the *off-resonance* frequencies (e.g., the curves for $R_l = 10^3 \Omega$ and $R_l = 10^4 \Omega$ intersect at 193.68 Hz). At these intersection frequencies, the two respective load resistance values yield the same power output.

We further investigate the variation of power output with load resistance for excitations at the short circuit and open circuit resonance frequencies of the first vibration mode through Fig. 8. It can be remembered from Figs. 4 and 6 that the voltage and the current outputs obtained at the short circuit resonance frequency are higher than the ones obtained at the open circuit resonance frequency up to a certain load resistance (approximately 39.8 k Ω in this case) after which the opposite is valid. Since the power output is simply the product of the voltage and current, this observation is also valid for the power versus load resistance curves. As can be seen from Fig. 8, we have the same intersection point ($R_l \approx 39.8$ k Ω) and the power output at the short circuit resonance frequency is higher before this point, whereas the power output at the open circuit resonance frequency is higher after this point. The trend in the low load resistance region is similar to that of the voltage output where the graphs increase with the same slope (in log-log scale) with increasing load resistance.

More importantly, since the behavior of power with changing load resistance is not monotonic, both of the power graphs shown in Fig. 8 display peak values, which correspond to the optimum values of load resistance. When the optimum values of load resistance are used for each of the cases (short circuit and open circuit

excitations), both of them yield the same power output. Considering Figs. 4 and 6, it can be observed that neither voltages nor currents are identical at these optimum values of load resistance for excitations at short circuit and open circuit resonance frequencies. However, the products of voltage and current for both cases are identical so that the power outputs for these resistive loads are identical for the short circuit and open circuit resonance frequency excitations separately.

7.5 Frequency Response of Beam Vibration. Now, we define the relative tip motion FRF (or the relative motion transmissibility function), which is the ratio of the vibration (displacement) amplitude at the tip of the beam (relative to the base) to the amplitude of the base displacement. Therefore, this mechanical FRF can be expressed using Eq. (51) as

$$\frac{w_{\text{rel}}(L, t)}{Y_0 e^{j\omega t}} = \sum_{r=1}^{\infty} \gamma_r^w - \chi_r \left(\frac{\sum_{r=1}^{\infty} \frac{j\omega \phi_r \gamma_r^w}{\omega_r^2 - \omega^2 + j2\zeta_r \omega_r \omega}}{\sum_{r=1}^{\infty} \frac{j\omega \chi_r \phi_r}{\omega_r^2 - \omega^2 + j2\zeta_r \omega_r \omega} + \frac{1 + j\omega \tau_c}{\tau_c}} \right) \times \frac{m\omega^2 \phi_r(L)}{\omega_r^2 - \omega^2 + j2\zeta_r \omega_r \omega} \quad (65)$$

Note that one could as well define the relative motion transmissibility FRF for any other point (say, for point x_1) throughout the beam (by simply setting $\phi_r(x_1)$ at the right hand side of Eq. (65)). However, the motion at the tip of the beam is of particular interest, because it is the position of the maximum transverse displacement for the practical vibration modes. As a consequence, the vibratory motion at the tip of the beam plays an important role while deciding on the volume of the harvester.

Figure 9 shows the modulus of the relative tip motion FRF against excitation frequency. Considering the main graph, it is not easy to distinguish between the FRFs for different values of load resistance. However, as can be seen from the enlarged views in Fig. 9, there are considerable variations around the resonance frequencies. We observe the same short circuit and open circuit resonance frequency behaviors. Note that the uncoupled (purely mechanical) FRF is also provided, and expectedly, as $R_l \rightarrow 0$, the coupled FRF converges to the uncoupled FRF.

As the value of load resistance is increased from $R_l = 10^2 \Omega$ to $R_l = 10^5 \Omega$, the vibration amplitude at the short circuit resonance frequency (47.8 Hz) decreases considerably (by a factor of about 2.5). However, when R_l is further increased to $10^6 \Omega$, the amplitude of vibrations at this frequency starts increasing. Therefore, it can be concluded that the vibration amplitude at a frequency does not necessarily show a monotonic behavior with increasing/decreasing load resistance, as in the case of the power output FRF. If we investigate the vibration amplitude at the open circuit resonance frequency (48.8 Hz) as R_l is increased from $10^2 \Omega$ to $10^6 \Omega$, we see that the vibration amplitude first starts decreasing smoothly and then it starts increasing sharply.

Figure 10 allows investigating the variation of relative tip displacement amplitude with load resistance more clearly. As can be seen from Fig. 10, the relative tip vibration is insensitive to variations of load resistance in the low load resistance region and reasonably the vibration amplitude at the short circuit resonance frequency is higher in this region. As the load resistance is further increased, due to the electromechanical effects, the vibration amplitude at the short circuit resonance frequency is attenuated. One should be aware of the fact that this attenuation in the vibration amplitude at the short circuit resonance frequency is indeed more complicated than just damping. Considering the first enlarged view in Fig. 9, one can see that the peak moves from 47.8 Hz to 48.8 Hz. This is the reason of the attenuation of vibration amplitude at 47.8 Hz. At this point, one should expect some increase in the vibration amplitude at 48.8 Hz and this is what we

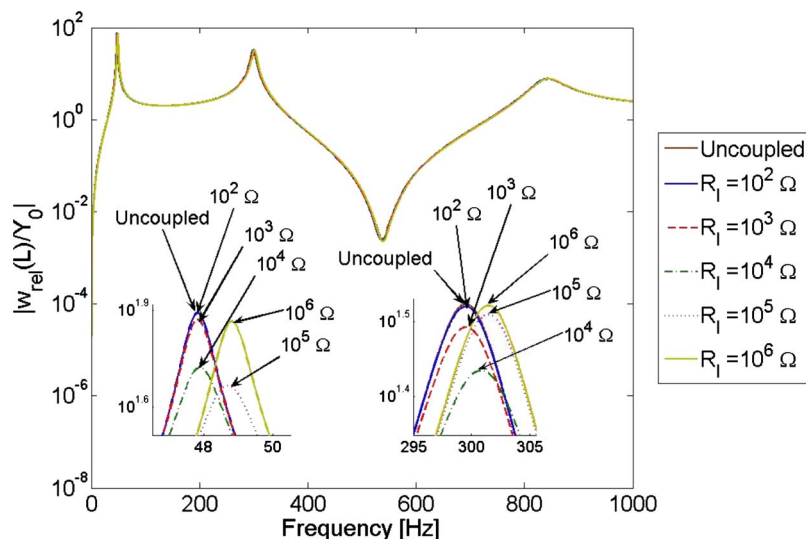


Fig. 9 Relative tip motion FRF for the uncoupled system and for the coupled system with five different values of load resistance (with the enlarged views of Mode 1 and Mode 2 resonances showing the short circuit and open circuit behaviors)

observe both in Figs. 9 and 10. As the load resistance increases, the peak, which used to be at the short circuit resonance frequency, moves toward the open circuit resonance frequency, causing not only an attenuation at the former frequency but also an increase at the latter frequency.

It is also worthwhile to investigate the power versus load resistance (Fig. 8) and the relative tip displacement versus load resistance (Fig. 10) trends simultaneously. At the short circuit resonance frequency, as the load resistance is increased gradually, the power output increases until the load resistance takes its optimum value. At the same time, the vibration amplitude is attenuated considerably. Further increase in the load resistance reduces the power output, which is associated with a slight increase in the vibration amplitude. At the open circuit resonance frequency, an increase in the load resistance first reduces the vibration amplitude slightly and the power increases at the same time. Then, in the vicinity of the optimum load resistance for excitation at open circuit resonance frequency, the vibration amplitude starts increasing

and it increases with increasing load resistance with a high rate. The important observation is the opposite trend in the relative tip displacement for excitations at the short circuit and the open circuit resonance frequencies around their respective optimum resistive loads.

It should be mentioned that the relative tip motion FRF exhibits *antiresonance* frequencies. In the frequency range 0–1000 Hz, an antiresonance frequency is captured at 536.7 Hz for short circuit conditions, which moves to 538.6 Hz for open circuit conditions. It can be seen from Fig. 9 that, at this antiresonance frequency, the relative displacement at the tip of the beam is less than 1% of the base displacement. Note that this is the formal definition of an antiresonance frequency of an FRF in the vibration literature and this frequency should not be confused with the open circuit frequency of a vibration mode, which duToit et al. [6] call the antiresonance frequency in their SDOF model. Although it is not possible to see from Fig. 9, the FRFs are not identical at the off-resonance frequencies and they are slightly different. The intersections between the curves observed for the power FRF are also observed here in the relative tip motion FRF.

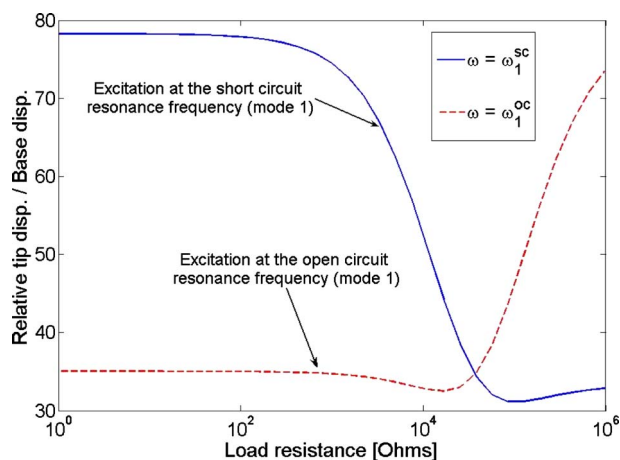


Fig. 10 Variation of relative tip displacement to base displacement ratio with load resistance for base excitations at the short circuit and open circuit resonance frequencies of the first vibration mode

8 Electromechanical Coupling and the Effect of Strain Nodes

Consider the general form of the circuit equation given by Eq. (34). The forcing term at the right hand side of this equation determines the amplitude of the electrical output. Other than the modal mechanical response (in the form of modal velocity response), the forcing term depends on the *modal coupling term* φ_r . As far as the mechanical equation of motion is concerned, the coupling information is included in the term χ_r , as can be seen from Eq. (27). Although φ_r and χ_r are defined separately in the electrical and the mechanical equations for convenience, they are not too different terms. Both φ_r and χ_r depend on the geometric parameters of the beam, Young's modulus, and the electromechanical parameters of the PZT, and more importantly, the *bending slope eigenfunction* evaluated at the boundaries of the electrodes. If the type of the PZT and the geometry of the composite harvester beam are already decided, the last term related to the bending slope plays a very important role in shaping the coupled dynamics of the electromechanical system.

In the main derivation, since we assumed the electrodes to be covering the entire length of the beam, the parameter related to the bending slope eigenfunction was reduced to the slope at the free end of the beam (because the slope at the root of the beam is already zero). If the electrodes cover only the arbitrary region $x_1 \leq x \leq x_2$, the term related to the bending slope eigenfunction appearing in the coupling term expressions, Eqs. (28) and (35), must be modified as follows:

$$\left. \frac{d\phi_r(x)}{dx} \right|_{x=L} \rightarrow \left. \frac{d\phi_r(x)}{dx} \right|_{x=x_2} - \left. \frac{d\phi_r(x)}{dx} \right|_{x=x_1} \quad (66)$$

which describes the dependence of electromechanical coupling on the locations of the electrodes for harvesting energy from the r th vibration mode. If the continuous electrodes are located such that the slopes at their boundaries are identical for a vibration mode, one should expect zero or very low electromechanical coupling for vibrations at that mode. It should be kept in mind that good electromechanical coupling yields good electrical outputs in energy harvesting. Therefore, for vibrations at a particular mode shape, the aim must be to keep the bending slope difference at the boundaries of the electrodes maximum so that the maximum electrical output is extracted from the system.

The physical reason is the existence of the *strain nodes* where the distribution of the bending strain throughout the length of the beam changes sign, i.e., its phase changes by 180 deg [12]. Strain nodes exist in all vibration modes other than the fundamental vibration mode of a cantilevered beam. Only in the first vibration mode, the strain distribution along the length of the beam is in phase. In all higher vibration modes, the *curvature* eigenfunction ($d^2\phi_r(x)/dx^2$) of the beam (which is a measure of bending strain) changes sign as we move from the clamped end to the free end of the beam. We observe from Eq. (35) that the electromechanical coupling is proportional to the integral of the curvature over the length of the electrodes. This is why we end up with the bending slope eigenfunction ($d\phi_r(x)/dx$) evaluated at the boundaries of the electrodes. Due to the sign change in the integrand, cancellation occurs and the electromechanical coupling and consequently the electrical outputs are reduced drastically. In order to avoid this cancellation, segmented electrode pairs must be used to collect the electric charge developed at the opposite sides of strain nodes. The resulting electrical outputs of these electrode pairs will be out of phase by 180 deg. and their leads must be combined accordingly for the maximum electrical output in the circuit [15].

We provide two simple demonstrations from our parametric case study given in the previous section for a specific resistive load ($R_l = 10^5 \Omega$). The first vibration mode has no strain nodes, whereas the second vibration mode has one strain node at $x = 0.216L$, and the third vibration mode has two strain nodes at $x = 0.132L$ and $x = 0.497L$ (remember that x is measured from the clamped end of the beam and L is the length of the beam). Furthermore, for the second mode shape, it can be obtained that the slope at $x = 0.471L$ is zero. For the third mode shape, one of the two positions where the slope is zero is $x = 0.291L$ [12]. Note that all these numbers are for an Euler–Bernoulli beam without a tip mass, and existence of a tip mass alters these numerical values [15].

Figure 11 shows three voltage FRFs for different electrode configurations and the attention is given to the second vibration mode. In the first configuration, the continuous electrode pair covers the entire surface of the beam ($0 < x < L$), which was already the case in our main discussion. We know that it gives the best electrical output for the first vibration mode since the strain distribution along the length of the beam is in phase for this mode. However, we also know that the second vibration mode has a strain node at $x = 0.216L$ and covering this point by continuous electrodes should cause some cancellation. In order to see this, we introduce the second configuration where the electrodes cover the region between the strain node of the second mode and the free

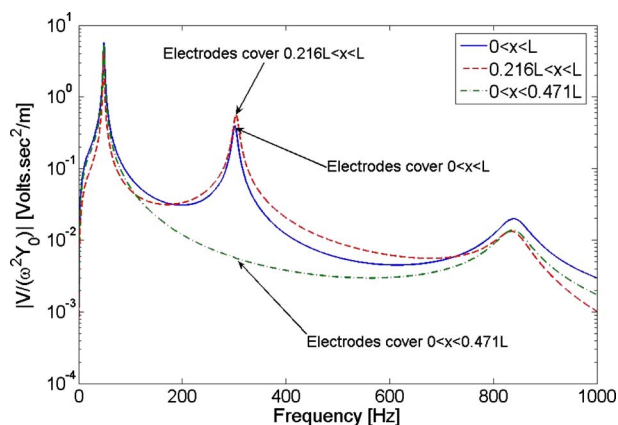


Fig. 11 Effect of the location of continuous electrode pair on the voltage FRF (focusing on the vibrations around the second mode)

end of the beam (that is, $0.216L < x < L$). As can be seen from Fig. 11, this configuration improves the voltage output from the second vibration mode (by a factor of more than 1.4). If desired, another electrode pair can be used to cover the region $0 < x < 0.216L$ and these two outputs (which are 180 deg out of phase) can be combined for the best output from the second vibration mode. The third configuration covers the region $0 < x < 0.471L$. The major strain distributions between $0 < x < 0.216L$ and $0.216L < x < 0.471L$ cancel each other, and as can be seen from Fig. 11, the resulting voltage output from the second vibration mode is reduced drastically for this configuration (by a factor of more than 70). The slight contribution comes from residues of the neighboring modes, particularly from the first mode. It should also be mentioned that, among these configurations, the first and the third vibration modes give the best voltage output for the first configuration where the entire surface of the beam is covered with continuous electrodes.

Next, consider Fig. 12 where the attention is given to the third vibration mode. Again, we consider three electrode configurations. The continuous electrode pair covers the entire length of the beam in the first configuration ($0 < x < L$). Although this configuration gives the highest voltage output for the first vibration mode, this is not the case for the third mode, which has two strain nodes at $x = 0.132L$ and $x = 0.497L$. In the second configuration, the electrodes cover the region between these strain nodes, which is

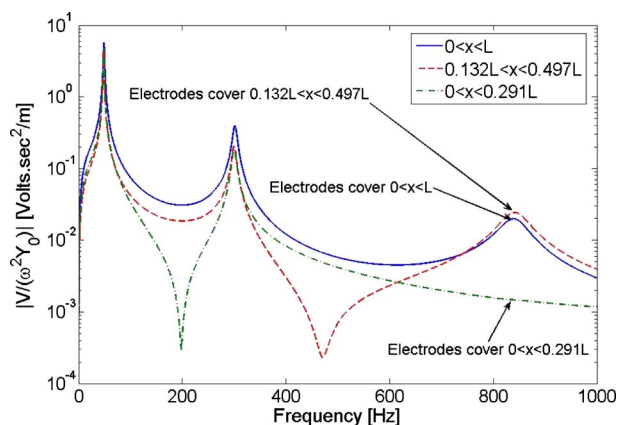


Fig. 12 Effect of the location of continuous electrode pair on the voltage FRF (focusing on the vibrations around the third mode)

$0.132L < x < 0.497L$. As can be seen from Fig. 12, this configuration improves the voltage output from the third mode (by a factor of more than 1.2). One might as well obtain the voltage outputs from the remaining regions $0 < x < 0.132L$ and $0.497L < x < L$, and combine all three outputs to obtain the maximum voltage output. Note that the voltage output from the electrode pair covering $0.132L < x < 0.497L$ will be 180 deg out of phase and the outputs of the other two regions will be in phase. In the third configuration, the electrodes cover the region $0 < x < 0.291L$ for demonstrating the cancellation in the third mode clearly. Since the strain distributions in $0 < x < 0.132L$ and $0.132L < x < 0.291L$ cancel each other, the voltage output is attenuated by a factor of more than 13. The slight electrical output is due to the contributions from the neighboring modes, especially from the second vibration mode. One should also notice the antiresonance frequencies that show up in the FRF for the second and the third electrode configurations.

9 Conclusions

In this paper, a distributed parameter electromechanical model for cantilevered piezoelectric harvesters is derived. The analytical formulation of the coupled system is based on Euler–Bernoulli beam assumptions. The harvester beam is assumed to be excited due to the translational motion of its base in the transverse direction with superimposed small rotation. In mechanical modeling, the internal strain rate damping (i.e., Kelvin–Voigt damping) and the external air damping are treated more accurately by defining separate damping coefficients.

The electromechanical equations are first derived for general transient base motions. In other words, the base motion is not restricted to be harmonic in time so that general coupled expressions for the mechanical response and voltage output are obtained. Then, the electromechanically coupled equations are reduced for the case of harmonic base translation with small rotation, and closed-form expressions are presented for the voltage, current, and power outputs as well as the coupled mechanical response of the harvester. The resulting equations are further reduced for the case of excitation around a natural frequency.

The analytically obtained expressions are then used in a parametric case study. In order to observe the frequency response behavior of the electrical outputs and the relative tip motion of the harvester, the FRFs which relate the voltage, current, power, and relative tip motion to the base motion are identified. These FRFs are plotted against frequency for a wide range of load resistance. Short circuit and open circuit conditions of the system are discussed. For a better understanding of short circuit and open circuit conditions, the electromechanical outputs are also plotted against load resistance for these two extreme cases of the resistive load. The mathematical modeling is based on the assumption of proportional damping (strain rate damping is assumed to be stiffness proportional, whereas air damping is assumed to be mass proportional). However, after describing how to identify the strain rate and air damping coefficients from experimental measurements, a simple relaxation is described for handling experimentally obtained nonproportional damping in the modal expansion.

Finally, electromechanical coupling and its relevance to the locations of the electrodes and the strain nodes are discussed. Once the geometry and the material of the bender are decided, the locations of the electrodes become important in determining the magnitude of the modal electromechanical coupling, which determines the magnitude of the electrical outputs. The issue of strain nodes of vibration mode shapes and cancellation of the electrical outputs due to covering the strain nodes of higher vibration modes with continuous electrodes are described with examples. Suggestions are made for increasing the electromechanical coupling and therefore the electrical outputs of the harvester.

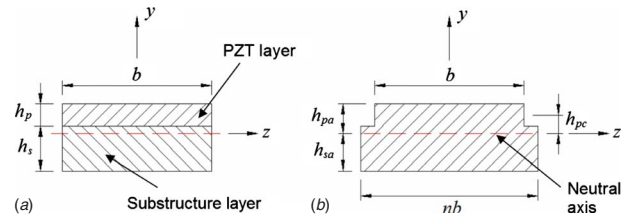


Fig. 13 (a) Cross section of a unimorph harvester and (b) the transformed cross section

Acknowledgment

The authors gratefully acknowledge the support of the Air Force Office of Scientific Research MURI under Grant No. F9550-06-1-0326 “Energy Harvesting and Storage Systems for Future Air Force Vehicles” monitored by Dr. B. L. Lee.

Appendix

Consider Fig. 13(a), which displays the cross section of the composite unimorph beam of Fig. 1. The width of the beam is denoted by b , the thickness of the PZT layer is h_p , and the thickness of the substructure layer is h_s . The procedure of finding the position of the neutral axis of a composite cross section is described in elementary strength of material texts (e.g., Timoshenko and Young [18]) and it requires transforming the cross section to a homogeneous cross section of single Young’s modulus (see Fig. 13(b)). We take the PZT as the material of the transformed cross section and define the ratio of Young’s moduli as $n = Y_s/Y_p$. In the transformed cross section, the width of the substructure layer is increased if $Y_s > Y_p$ or it is reduced if $Y_p > Y_s$. For demonstration, the typical case $Y_s > Y_p$ is assumed in Fig. 13(b) (which is also the case in our parametric case study) so that widening occurs in the substructure layer. Then, it is a simple practice to obtain the parameters defined in Fig. 13(b) (and therefore the position of the neutral axis) in terms of the parameters of Fig. 13(a) and Young’s moduli ratio n as follows:

$$h_{pa} = \frac{h_p^2 + 2nh_ph_s + nh_s^2}{2(h_p + nh_s)}, \quad h_{sa} = \frac{h_p^2 + 2h_ph_s + nh_s^2}{2(h_p + nh_s)}, \quad (A1)$$

$$h_{pc} = \frac{nh_s(h_p + h_s)}{2(h_p + nh_s)}$$

where h_{pa} is the distance from the top of the PZT layer to the neutral axis, h_{sa} is the distance from the bottom of the substructure layer to the neutral axis, and h_{pc} is the distance from the center of the PZT layer to the neutral axis. Note that the geometric parameters used in the main formulation (h_a , h_b , and h_c) describe positions from the neutral axis rather than distances. Therefore, they can be expressed as

$$h_a = -h_{sa}, \quad h_b = h_{pa} - h_p, \quad h_c = h_{pa} \quad (A2)$$

It can be remembered from the main text that h_a is the position of the bottom of the substructure layer from the neutral axis (always negative), h_b is the position of the bottom of the PZT layer from the neutral axis (positive or negative), and h_c is the position of the top of the PZT layer from the neutral axis (always positive).

References

- [1] Anton, S. R., and Sodano, H. A., 2007, “A Review of Power Harvesting Using Piezoelectric Materials (2003–2006),” *Smart Mater. Struct.*, **16**, pp. R1–R21.
- [2] Sodano, H. A., Park, G., and Inman, D. J., 2004, “Estimation of Electric Charge Output for Piezoelectric Energy Harvesting,” *Strain J. Brit. Soc. Strain Measurement*, **40**, pp. 49–58.
- [3] duToit, N. E., and Wardle, B. L., 2006, “Experimental Verification of Models for Microfabricated Piezoelectric Vibration Energy Harvesters,” *Proceedings of the 47th AIAA/ASME/ASCE/AHS/ASC Structures, Structural Dynamics, and*

- Materials Conference*, Newport, RI, pp. 1–20.
- [4] Jeon, Y. B., Sood, R., Jeong, J. H., and Kim, S., 2005, “MEMS Power Generator With Transverse Mode Thin Film PZT,” *Sens. Actuators, A*, **122**, pp. 16–22.
 - [5] Roundy, S., Wright, P. K., and Rabaey, J. M., 2003, “A Study of Low Level Vibrations as a Power Source for Wireless Sensor Nodes,” *Comput. Commun.*, **26**, pp. 1131–1144.
 - [6] duToit, N. E., Wardle, B. L., and Kim, S., 2005, “Design Considerations for MEMS-Scale Piezoelectric Mechanical Vibration Energy Harvesters,” *Integr. Ferroelectr.*, **71**, pp. 121–160.
 - [7] Lu, F., Lee, H. P., and Lim, S. P., 2004, “Modeling and Analysis of Micro Piezoelectric Power Generators for Micro-Electromechanical-Systems Applications,” *Smart Mater. Struct.*, **13**, pp. 57–63.
 - [8] Chen, S.-N., Wang, G.-J., and Chien, M.-C., 2006, “Analytical Modeling of Piezoelectric Vibration-Induced Micro Power Generator,” *Mechatronics*, **16**, pp. 397–387.
 - [9] Ajitsaria, J., Choe, S. Y., Shen, D., and Kim, D. J., 2007, “Modeling and Analysis of a Bimorph Piezoelectric Cantilever Beam for Voltage Generation,” *Smart Mater. Struct.*, **16**, pp. 447–454.
 - [10] Stephen, N. G., 2006, “On Energy Harvesting From Ambient Vibration,” *J. Sound Vib.*, **293**, pp. 409–425.
 - [11] Fang, H.-B., Liu, J.-Q., Xu, Z.-Y., Dong, L., Chen, D., Cai, B.-C., and Liu, Y., 2006, “A MEMS-Based Piezoelectric Power Generator for Low Frequency Vibration Energy Harvesting,” *Chin. Phys. Lett.*, **23**, pp. 732–734.
 - [12] Erturk, A., and Inman, D. J., 2008, “On Mechanical Modeling of Cantilevered Piezoelectric Vibration Energy Harvesters,” *J. Intell. Mater. Syst. Struct.* in press, doi: 10.1177/1045389X07085639.
 - [13] 1987, *IEEE Standard on Piezoelectricity*, IEEE, New York.
 - [14] Williams, C. B., and Yates, R. B., 1996, “Analysis of a Micro-Electric Generator for Microsystems,” *Sens. Actuators, A*, **52**, pp. 8–11.
 - [15] Erturk, A., Farmer, J. R., and Inman, D. J., “Effect of Strain Nodes and Electrode Configuration on Piezoelectric Energy Harvesting From Cantilevered Beams,” *J. Vibr. Acoust.*, submitted.
 - [16] Timoshenko, S., Young, D. H., and Weaver, W., 1974, *Vibration Problems in Engineering*, Wiley, New York.
 - [17] Caughey, T. K., and O’Kelly, M. E. J., 1965, “Classical Normal Modes in Damped Linear Dynamic Systems,” *ASME J. Appl. Mech.*, **32**, pp. 583–588.
 - [18] Timoshenko, S., and Young, D. H., 1968, *Elements of Strength of Materials*, Van Nostrand Reinhold, New York.
 - [19] Schwartz, L., 1978, *Théorie des Distributions*, Hermann, Paris, France.
 - [20] Erturk, A., and Inman, D. J., 2007, “Mechanical Considerations for Modeling of Vibration-Based Energy Harvesters,” *Proceedings of the ASME IDETC 21st Biennial Conference on Mechanical Vibration and Noise*, Las Vegas, NV, Sep. 4–7.
 - [21] Moheimani, S. O. R., Fleming, A. J., and Behrens, S., 2002, “On the Feedback Structure of Wideband Piezoelectric Shunt Damping Systems,” *Smart Mater. Struct.*, **12**, pp. 49–56.
 - [22] Clough, R. W., and Penzien, J., 1975, *Dynamics of Structures*, Wiley, New York.